REYNOLDS NUMBER EFFECTS OF INTERNAL SOLITARY WAVES PROPAGATING ON A UNIFORM SLOPE

HAI ZHU

College of Water Conservancy and Hydropower Engineering, Hohai University, Nanjing, China, h.zhu@hhu.edu.cn

SONGPING MAO

College of Water Conservancy and Hydropower Engineering, Hohai University, Nanjing, China, 191302010022@hhu.edu.cn

DECAI SUN

Huai'an Water Conservancy Survey Design Research Institute Co., Ltd., Huai'an, China, 287241099@qq.com

LINGLING WANG

College of Water Conservancy and Hydropower Engineering, Hohai University, Nanjing, China, wanglingling@hhu.edu.cn

ZHENZHEN YU

Water Resources Protection and Research Institute, Yellow River Basin Water Resources Protection Bureau, Zhengzhou, China, 749928067@qq.com

CHENG LIN

Department of Civil Engineering, National Chung Hsing University, Taizhong, China, chenglin@dragon.nchu.edu.tw

ABSTRACT

Internal solitary waves (ISWs) ubiquitously exist in oceans and they also frequently occur in density stratified lakes. Numerous laboratory-scale physical experiments and numerical simulations have been carried out to explore the shoaling dynamics of ISWs on slope topographies. Detailed features during wave breaking have been investigated under relatively low Reynolds numbers, but for real ocean-scale or lake-scale scenarios with a much higher Reynolds number, laboratory-scale modeling is inadequate to capture the three-dimensional turbulent characteristics in the wave shoaling process. As a result, the Reynolds number effects during the shoaling process of ISWs traveling on uniform slopes are investigated by 3D numerical simulations. Scale effects due to different Reynolds numbers and three-dimensional characteristics during wave shoaling are explored and discussed. It is found that the maximum wave-induced velocities and energy loss are well related to Iribarren numbers and the extreme velocities, wave energy loss, and three-dimensionality of the flow field are all identified to be very sensitive to Reynolds numbers, indicating that traditional two-dimensional laboratory-scale modeling tools may be insufficient to accurately capture the shoaling mechanisms of ISWs.

Keywords: Internal solitary waves, shoaling process, internal wave breaking, Reynolds number effects

1. INTRODUCTION

Internal solitary waves (ISWs) widely exist in oceans (Moum et al., 2007; Duda et al., 2004) where they are usually generated from tide-topography interaction. Nonlinear ISWs are also ubiquitous in seasonal stratified lakes and wind force are usually the primary driven forces (Sakai and Redekopp, 2010). Even in relatively small lakes, internal waves re-occur frequently and can have potential ecological consequences for metalimnetic phytoplankton populations (Pannard et al., 2011). Shoaling ISWs and the corresponding breaking mechanisms have great impact on the mixing in the interior of oceans and lakes, on sediment re-suspension and nutrients transport. Intensive in-situ observations of nonlinear internal waves on the Portuguese shelf showed that internal waves provided an important source of vertical mixing (Jeans and Sherwin, 2001). Numerous laboratory experiments have been carried out to study the shoaling process of ISWs. Helfrich (1992) observed the shoaling of a single ISW can break and produce multiple turbulent surges, resulting in significant vertical mixing occurring everywhere inshore of the breaking location. The shoaling and breaking of an internal solitary wave of depression on a uniform slope were studied experimentally by Michallet and Ivey (1999). They pointed out that even if the mixing efficiency was low for a particular ISW shoaling process, the regular nature of the breaking event was important for the mixing and transport of benthic materials over long periods of time. Internal solitary wave evolution was performed on steep and inverse uniform slopes by Chen et al. (2007) and a mirror-image model was hypothesized to describe the physical features of shoaling waves. As evidently pointed out by Guo and Chen (2014), the ISWs of

depression type can convert into the elevation counterparts while traveling toward continental slopes/shelves. This evidence strongly indicates that more frequent occurrences of the shoaling process for the ISWs of elevation type can be expected in nature. For instance, the depression-typed ISWs in the northeastern South China Sea were observed to transform into the elevation counterparts over the seafloor of about 100 ~ 200 m deep (Bai et al. 2017).

As obviously shown by Aghsaee et al. (2010), collapsing or collapsing-plunging breakers during the shoaling process for the depression-typed ISWs do convert into plunging breakers for higher Reynolds number cases. It would be interesting to study the Reynolds number effects for the interaction between the elevation-typed ISWs and uniform slopes under a three-dimensional frame. The main purpose of the present study is thus to investigate the highly unsteady turbulent process and the scale effects during ISW-slope interaction based on three-dimensional large eddy simulation (LES).

2. NUMERICLA MODELS

2.1 Governing equations

A three-dimensional LES has been employed in the present study to explore the detailed dynamics of ISW-slope interaction. The physical process is governed by the filtered continuity and Navier-Stokes equations,

$$\frac{\partial \overline{u_i}}{\partial x_i} = 0 \tag{1}$$

$$\frac{\partial \overline{u_i}}{\partial t} + \overline{u_i}\frac{\partial \overline{u_j}}{\partial x_i} = -\frac{1}{\rho}\frac{\partial \overline{p}}{\partial x_i} + (v + v_t)\frac{\partial^2 \overline{u_i}}{\partial x_j \partial x_j} + \overline{f_i} \tag{2}$$

where $\overline{u_i}$ is the filtered velocity component, x_i is the Cartesian coordinate, ρ is the density of the fluid, $\overline{p}$ is the pressure, v is the kinematic viscosity and $\overline{f_i}$ is the body force modelling the gravitational acceleration in the vertical direction. The Einstein summation convention and notation are used here. In addition, v_t is the eddy viscosity which can be modeled by the classic Smagorinsky subgrid-scale stress model:

$$v_t = (C_s \Delta)^2 \sqrt{2\overline{S_{ij}}\,\overline{S_{ij}}} \tag{3}$$

where C_s is the Smagorinsky constant, set to be 0.1 in the present study. Δ is the filtered length and S_{ij} is the rate of strain tensor identifying the symmetric part of the velocity gradient tensor. One of the factors that drives the ISWs' propagation is the density difference inside the fluid, and thus mass transfer between the two-layer water system is taken into account. The scalar transport equation that governs the advection-diffusion effect is as follows:

$$\frac{\partial \overline{c}}{\partial t} + \overline{u_i}\frac{\partial \overline{c}}{\partial x_i} = \frac{\partial}{\partial x_i}\left[(k + k_t)\frac{\partial \overline{c}}{\partial x_i}\right] \tag{4}$$

where c is the volume concentration of saline water in the fluid, k is the molecular diffusivity coefficient of the solute and k_t is the eddy diffusivity coefficient. The relationship between k_t and v_t can be linked with a turbulent Schmitt number Sc_t, $k_t = v_t/Sc_t$ with $Sc_t = 1.0$ in the present work.

2.2 Numerical methods

An in-house code called CgLES (Complex Geometry Large-eddy Simulation) originally developed by Thomas and Williams (1995) was applied here. Adams-Bashforth scheme of second order accuracy is used in time marching and a second order central difference scheme is used in space for the momentum equation discretization. The pressure Poisson equation is solved by a preconditioned pressure conjugated gradient method. Once the correct velocity field is obtained, the scalar transport equation is then solved. In time a conservative explicit second order Runge-Kutta scheme is used to discretize the advection-diffusion equation. The advection term itself is discretized by a second order upwind difference scheme while the diffusion term is discretized using second order central differences. The superbee flux limiter is used in the upwind scheme to ensure the solutions are total variation diminishing (TVD).

2.3 Model validation

The present numerical model CgLES has been successfully applied in the simulation of turbulent channel flows (Thomas and Williams 1995), interactions between ISWs and submerged ridges (Zhu et al. 2016). The detailed model validation can be found in the paper of Zhu et al. 2017, in which breaking of depression-typed ISWs on slopes was investigated.

3. SIMULATION SETUP AND COMPUTATIONAL CASES

3.1 Simulation setup

A three-dimensional computational domain is constructed to investigate the interaction between the elevation-typed ISWs and the uniform slopes. As is shown in Figure 1, the numerical wave tank has a dimension of 1500 m × 100 m × 50 m (L × H × W) in the horizontal (X), vertical (Y) and span-wise (Z) directions, respectively with the origin (X, Y) = (0, 0) m being located at the left bottom corner of the tank. The computational domain is stratified in two layers with a thin pycnocline in the middle. The two-layer fluid system consists of the upper-layer and lower-layer thicknesses of h_1 = 87.5 m and h_2 = 12.5 m with densities of ρ_1 = 1000 kg/m^3 and ρ_2 = 1030 kg/m^3, respectively. In the present work, the initial background stratification is configured as a smooth *tanh* profile in the vertical direction.
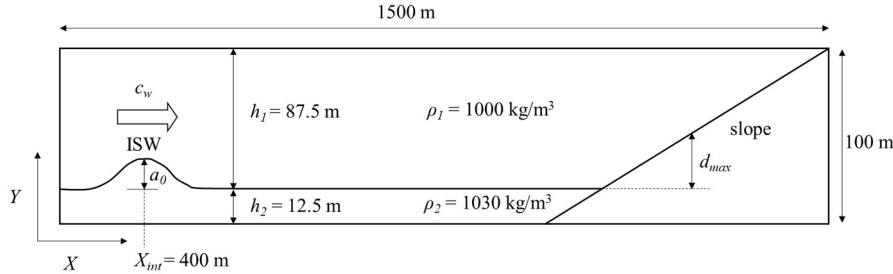

Figure 1. Schematic view of the numerical wave tank. The incident ISW propagates from left to right with the initial crest center located at X_{int} = 400 m.

3.2 Computational cases

As listed in Table 1, a total of 12 cases have been carried out to study the dynamics of elevation-typed ISWs shoaling on uniform slopes with different angles, θ, or slopes, s. The internal Iribarren number (I_r) in the table is defined as the ratio of the topographic slope s, and the square root of the incident wave steepness s_w. The initial wave amplitudes a_0 are set to be 12.5 m for all the cases. To explore the Reynolds number effects for the ISW-slope interaction, the order of magnitude of the wave Reynolds number Re_w is set to be about 10^3, 10^4 and 10^5 for case groups A, B and C respectively, through adjusting the kinematic viscosity v. Simulations are initialized according to the exact solitary wave solutions of the eKdV equation. For the case groups A with relatively lower Re_w, a mesh of 768 × 128 × 24 is used. For the cases B with medium Re_w and C with high Re_w, the grid resolutions are determined to be 1024 × 192 × 36 and 1536 × 256 × 48, respectively, after grid independent tests. Parallel computing was applied for all the computational cases with about 20, 60 and 500 CPU hours being consumed for case groups A, B and C respectively.

Table 1. Computational cases and related parameters

Case Group	a_0 (m)	Re_w ($a_w c_w/v$)	θ= 5° s = 0.087	θ= 10° s = 0.176	θ= 15° s = 0.268	θ= 20° s = 0.364
			Run No./Bolus formation/I_r			
A	12.5	$O(10^3)$	1/Y/0.197	2/Y/0.409	3/Y/0.631	4/N/0.867
B	12.5	$O(10^4)$	1/Y/0.196	2/Y/0.403	3/Y/0.617	4/N/0.842
C	12.5	$O(10^5)$	1/Y/0.195	2/Y/0.400	3/Y/0.613	4/N/0.838

4. RESULTS AND DISCUSSION

4.1 Dynamics of internal boluses

For case A1, a typical well-organized internal bolus develops during the upslope-surging process, as illustrated in Figure 2 in which T^* is the non-dimensional time (= $t^* c_w/h_2$) and T^* = 0 (or t^* = 0 s) is designated to be the moment when the crest of the incident ISW is exactly passing the toe of the uniform slope. It is meaningful to explore the formation process and propagation properties of the boluses because the formation of the internal boluses surging upslope during ISW-slope interaction can transport denser lower-layer fluid onshore, thus enhancing local mixing and dissipation. The bolus first emerges at T^* = 14.59 in the wave front characterized with an abrupt thicker blob of denser water having a maximum vertical excursion of d_b [see Figure 2(a)]. The foremost point also called the nose of the bolus [as marked in Figure 2(a)] is slightly above the slope with a height of h_b. Due to its larger mass inertial, the bolus tends to propagate faster than the ambient heavier fluid and gradually separates from the wave front at T^* = 18.24 [Figure 2(b)]. The main body of the incident ISW reflects from the slope but the bolus continues running up the slope [see Figure 2(c-f)]. The solid lines surrounding the bolus represent the density ISO-surface of $(\rho_1 + \rho_2)/2$. As clearly observed, the bolus shrinks its size gradually with time since the interior denser fluid continuously leaks out from the rear of the bolus. At T^* = 38.3, denser fluid above the average density (1015 kg/m^3) only concentrates in the core of

the bolus [Figure 2(e)]; and subsequently at $T^* = 43.78$, the maximum density inside the bolus is well below 1015 kg/m³ [Figure 2(f)].

(a) $T^* = 14.59$ (b) $T^* = 18.24$ (c) $T^* = 25.54$

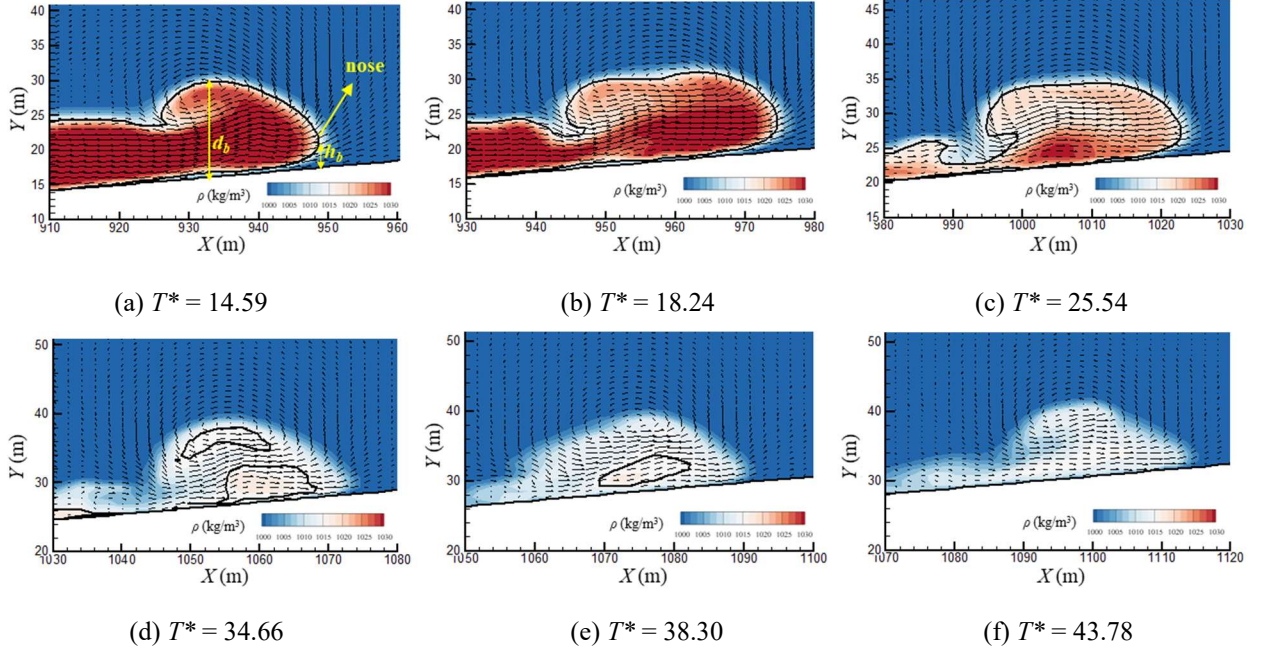(d) $T^* = 34.66$ (e) $T^* = 38.30$ (f) $T^* = 43.78$

Figure 2. Temporal and spatial variations of the internal bolus during ISW-slope interaction for case A1. Black solid curves correspond to the ISO-density line of $(\rho_1+\rho_2)/2$.

The average velocity of the upslope-surging bolus, U_b, is calculated based on the distance through which the nose can travel during the time interval from the incipient occurrence of a well-developed bolus to the instant that the nose reaches the maximum height. Herein, U_b is normalized by the incident wave phase speed c_w, thus leading to the so-called bolus Froude number, Fr_b ($= U_b/c_w$). It is interesting to note that Fr_b is closely related with I_r. Lower values of I_r represent the ISWs shoaling on milder slopes, larger-scale boluses with relatively huge kinetic energy would form and thus result in higher Fr_b. On the contrary, for the cases with higher values of I_r on steeper slopes, this situation reverses as evidently shown in Figure 3. For all the simulation cases in the present study, the maximum of Fr_b is 0.6 while the minimum is halved to be 0.3. The relationship between Fr_b and I_r is fitted by the following regressed curve,

$$Fr_b = 0.2\, I_r^{-0.59} \tag{5}$$

It should be noted that the corresponding relationship for medium and high Re_w case groups (marked by solid squares for cases B with $Re_w \sim 10^4$ and triangles for cases C with $Re_w \sim 10^5$) in Figure 3 also follow the same tendency with the fitted curve.
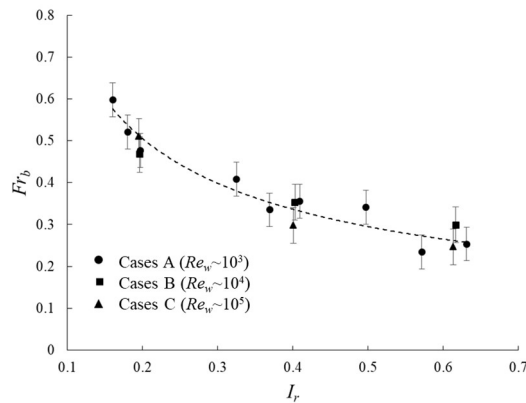

Figure 3. The relationship between Fr_b and I_r. The dashed line is fitted by the results from low Re_w case groups A, B and C with occurrence of the boluses. The vertical error bar is 15%.

4.2 Reynolds number effects

4.2.1 Maximum vertical displacement

Figure 4 shows the non-dimensional maximum vertical displacement d_{max}/a_w for ISWs shoaling on slopes with the vertical error bars of 2.5%. It means that the differences for d_{max}/a_w are less than 2.5% for all the cases with Re_w ranging two orders of magnitude higher, revealing nearly without Re_w effect on the distribution of d_{max}/a_w.
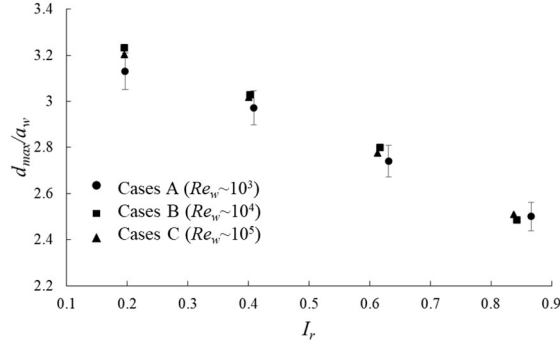
4

Figure 4. Non-dimensional maximum vertical displacement d_{max}/a_w versus I_r under differentReynolds numbers Re_w. The vertical error bar is 2.5%.

4.2.2 Maximum wave-induced velocities

However, the non-dimensional maximum wave-induced velocities (with $U^* = u_{max}/c_w$ and $V^* = v_{max}/c_w$) are more sensitive to Re_w because higher Re_w generally implies more prominent inertia and relatively larger flow velocities. As seen in the lower part of Figure 5(a), the non-dimensional maximum offshore velocities U^*_- does increase about 20% if Re_w becomes one order of magnitude higher. On the other hand, for the non-dimensional maximum onshore velocities U^*_+, although higher Re_w corresponds to higher velocity magnitudes, the velocity increment is about 20% if Re_w is varied from 10^3 to 10^5 [see the upper part in Figure 5(a)]. It is also found that V^*_+ and U^*_- are more sensitive to Re_w for lower and higher values of I_r, respectively. In addition, the non-dimensional maximum vertical velocities U^*_+ and U^*_- have significant increase if Re_w is increased two orders of magnitude higher for higher I_r cases [see Figure 5(b)].

The above characteristics of the extreme velocity under different Re_w are found to be related with their spatial distribution. Detailed statistics shows that the locations at which the maximum non-dimensional velocity U^* and V^* occur can either be in the bolus, in the upslope surging process prior to bolus formation or in the boundary jet during the ISW run-down process (marked with green, red and blue in Figure 5 respectively). The positions where the maximum horizontal velocity U^* emerges show less independency of Re_w numbers. The maximum horizontal onshore velocities U^*_+ always occur during the upslope surging process while the occurrence of its offshore counterpart U^*_- is always in the boundary jet during the flowing down process [in Figure 5(a)]. On the other hand, the locations with the maximum vertical velocity V^* are closely linked with Re_w numbers, especially for higher I_r cases [in Figure 5(b)]. For lower I_r (~ 0.2), the maximum vertical velocity V^* tends to occur inside the bolus for Re_w ranges from 10^3 to 10^5. However, for I_r ~ 0.4, the maximum upward vertical velocity V^*_+ is found inside the bolus for $Re_w = 10^3 \sim 10^4$, but is induced by the boundary jet for $Re_w \sim 10^5$. For even higher I_r cases without bolus formation, the location of V^*_+ is in the upslope surge under low and medium Re_w, but can be shifted to the boundary jet under higher Re_w. The location of V^*_- is limited in the boundary jet, reflecting the characteristic of Re_w number independency.
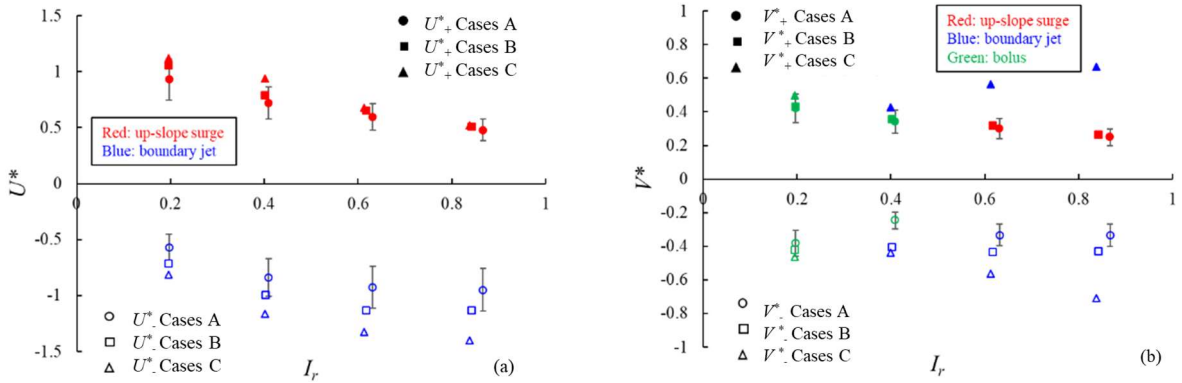

Figure 5. Extreme velocities during the ISW-slope interaction under different Reynolds numbers. Note that different colors correspond to different locations where the peak velocity occurs. The vertical error bar is 20%.

4.2.3 Wave energy loss

During the ISW run-up process, including the upslope surge and the afterwards bolus evolution, a majority part of kinetic energy (KE) of the incident ISW gradually converts into available potential energy (APE). Taking case A4 during the ISW run-up phase as an example, due to the transformation into APE and dissipation, as high as around 90% of the KE can be reduced, indicating a suppressed or restrained Re_w

number effect. As a result, peak velocities inside the bolus or in the upslope surge (marked in green and red respectively in Figure 5) are generally insensitive to Re_w numbers compared with their counterparts in the boundary jet. On the contrary, when APE converts into KE during the ISW run-down phase, inertial force dominates again due to the conversion of APE to KE, and thus peak velocities inside the boundary jet are closely influenced by Re_w.

The non-dimensional energy loss δE during the ISW shoaling process is also sensitive to Re_w. Higher Re_w indicates smaller viscous effect and relatively less energy loss, as shown in Figure 6. Especially for cases with $I_r > 0.5$, the energy loss can decrease more than 20% if Re_w increases from 10^3 to 10^4.
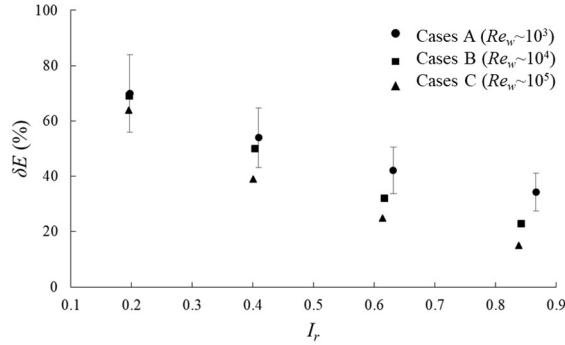

Figure 6. Non-dimensional energy loss for the ISW-slope interaction under different Reynolds numbers. The vertical error bar is 20%

4.2.4 Three-dimensional effect

To explore the 3D coherent vortex structure inside the internal boluses, Q-criterion is employed for vortex identification and visualization. Figure 7(b-d) shows the instantaneous snapshots of the 3D vortex structures, extracted from the flow field when the maximum fluctuating velocity w' occurs for case A1, B1 and C1, respectively. The gray ISO-surface corresponds to $Q = 0.002$ s^{-1} and the blue region is identified as the vortex core inside the bolus with a much higher value ($Q = 0.02$ s^{-1}). For the ISW-slope interaction with the internal boluses, the flow field evolves from 2D to 3D due to the secondary instability. Figure 7 (a, b) shows the vortex structure with the transition process of vortex tubes from 2D to 3D for case AL1 with a lower Re_w at $T^* = 25.54$ and 34.66, respectively [also see Fig. 2(c, d)]. More irregular smaller-scale vortices can be observed for cases with medium and higher Re_w [see Figure 7 (c, d)]. Consequently, the 3D effect during the elevation-typed ISW shoaling on the slopes cannot be neglected even in laboratory-scale scenarios and 2D numerical simulations may be insufficient to capture the important 3D structures especially for the cases with bolus formation.
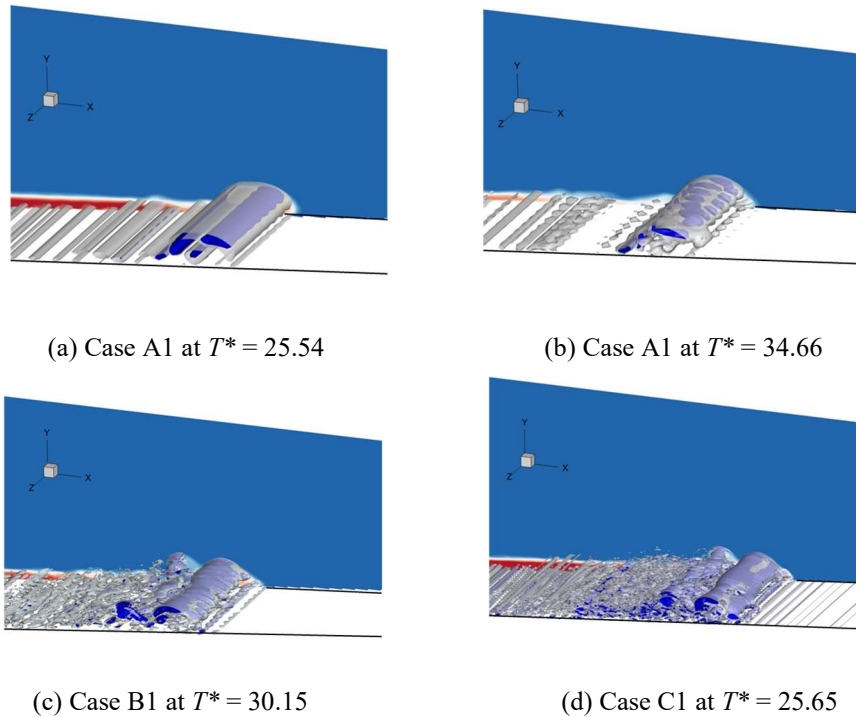

(a) Case A1 at $T^* = 25.54$ (b) Case A1 at $T^* = 34.66$

(c) Case B1 at $T^* = 30.15$ (d) Case C1 at $T^* = 25.65$

Figure 7. Instantaneous snapshots of 3D vortex structures within the internal bolus are plotted as the iso-surfaces of Q for cases A1, B1 and C1 while the instantaneous fluctuating velocity w' reaches the maximum. The gray and blue iso-surfaces correspond to $Q = 0.002$s^{-1} and $Q = 0.02$s^{-1}, respectively.

5. CONCLUSIONS

A highly resolved three dimensional large-eddy simulation (LES) has been carried out in the present work to investigate the less studied dynamics of the ISWs of elevation type shoaling on uniform slopes in a two-layer fluid system. A total number of 12 cases have been performed from laboratory-scale simulations with relatively low Reynolds numbers to the scenarios in which the Reynolds numbers are increased two orders of magnitude higher. Major conclusions of the present study can be drawn as follows:

(1) A well-organized internal bolus develops during the ISW shoaling process. The bolus Froude number is closely related with Iribarren number. Lower values of Iribarren number can result in a higher bolus Froude number.

(2) The maximum vertical displacement of the denser fluid and the propagation speed of the boluses is insensitive to the increase of Reynolds numbers. However, increasing the Reynolds numbers two orders of magnitudes higher can significantly increase the maximum wave-induced velocities and decrease the total wave energy loss during the shoaling process.

(3) The transition process of the flow field from 2D to 3D can be excited much faster during ISW-slope interaction for the cases with higher Reynolds numbers. Even for laboratory-scale simulations, 3D impact does exist although it may be relatively weak. Special caution should be paid to the situation if 2D models are employed for cases with bolus formation. Due to the significant Reynolds number effects during ISW-slope interaction, results from laboratory scale experiments and numerical simulations may not be suitable when extended to field scale applications.

REFERENCES

Aghsaee, P., Boegman, L. and Lamb, K. G. (2010). Breaking of shoaling internal solitary waves. *Journal of Fluid Mechanics*, 659: 1-29.

Bai, Y., Song, H., Guan, Y. and Yang, S. (2017). Estimating depth of polarity conversion of shoaling internal solitary waves in the northeastern South China Sea. *Continental Shelf Research*. 143: 9-17.

Chen C., Hsu J. and Cheng M. et al. (2007). An investigation on internal solitary waves in a two-layer fluid: Propagation and reflection from steep slopes. *Ocean Engineering*, 34: 71-184.

Guo, C., Chen, X. (2014). A review of internal solitary wave dynamics in the northern South China Sea. *Progress in Oceanography*, 121(2): 7-23.

Helfrich, K. R. (1992). Internal solitary wave breaking and run-up on a uniform slope. *Journal of Fluid Mechanics*, 243: 133-154.

Jeans, D. R. G. and Sherwin, T. J. (2001). The evolution and energetics of large amplitude nonlinear internal waves on the Portuguese shelf. *Journal of Marine Research*, 59: 327-53.

Michallet, H. and Ivey, G. N. (1999). Experiments on mixing due to internal solitary waves breaking on uniform slopes. *Journal of Geophysical Research*, 104(C6): 13467-13477.

Moum, J. N., Klymak, J. M. and Nash, J. D. et al. (2007). Energy transport by nonlinear internal waves. *Journal of Physical Oceanography*, 37: 1968-1988.

Pannard, A., Beisner, B. E. and Bird, D.F. et al. (2011). Recurrent internal waves in a small lake: potential ecological consequences for metalimnetic phytoplankton populations. *Limnology and Oceanography: Fluids and Environments*, 1: 91-109.

Sakai, T. and Redekopp, L. G. (2010). A parametric study of the generation and degeneration of wind-forced long internal waves in narrow lakes. *Journal of Fluid Mechanics*, 645: 315-344.

Thomas, T. G. and Williams, J. J. R. (1995). Turbulent simulation of open channel flow at low Reynolds number. *International Journal of Heat and Mass Transfer*. 38 (2): 259-266.

Zhu, H., Wang, L., Avital, E., Tang, H. and Williams, J. J. R. (2016). Numerical simulation of interaction between internal solitary waves and submerged ridges. *Applied Ocean Research*. 58:118-134.

Zhu, H., Wang, L., Avital, E., Tang, H. and Williams, J. J. R. (2017). Numerical simulation of shoaling broad-crested internal solitary waves. *Journal of Hydraulic Engineering*. 143 (6): 04017006.